

Voltage-Induced Inversion of Band Bending and Photovoltages at Semiconductor/Liquid Interfaces

Ruoxi Li, Marcos Gabriel Yoc-Bautista, Sizhe Weng, Zhi Cai, Bofan Zhao, and Stephen B. Cronin*



Cite This: <https://doi.org/10.1021/acsami.3c14116>



Read Online

ACCESS |



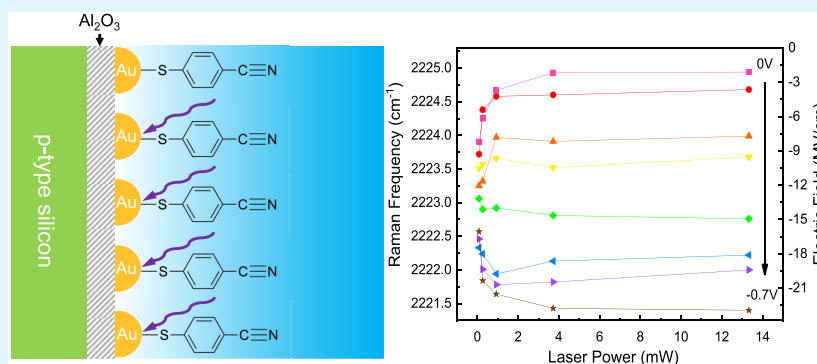
Metrics & More



Article Recommendations



Supporting Information



ABSTRACT: At semiconductor/liquid interfaces, the surface potential and photovoltages are produced by a combination of band bending and quasi-Fermi-level splitting at the semiconductor surface, which are usually treated in a qualitative fashion. As such, it is important to develop quantitative metrics for the band energies and photovoltaics at these interfaces. Here, we present a spectroscopic method for monitoring the photovoltages produced at semiconductor/liquid junctions. The surface reporter molecule mercaptobenzonitrile (MBN) is functionalized on the photoelectrode surface (p-type silicon) and is measured using *in situ* surface-enhanced Raman scattering (SERS) spectroscopy with a water immersion lens under electrochemical working conditions. In particular, the vibrational frequency of the C≡N stretch mode (ω_{CN}) around 2225 cm^{-1} is sensitive to the local electric field in solution at the electrode/electrolyte interface via the vibrational Stark effect. Over the applied potential range from -0.8 to 0.6 V vs Ag/AgCl, we observe ω_{CN} to increase from 2220 to 2229 cm^{-1} (at low laser power). As the incident laser power is increased from 83.5 μW to 13.3 mW, we observe additional shifts of $\Delta\omega_{\text{CN}} = \pm 1$ cm^{-1} , corresponding to photovoltages produced at the semiconductor/liquid interface $\Delta V = \pm 0.2$ V. Based on Mott–Schottky measurements, the flat band potential (FBP) occurs at -0.39 V vs Ag/AgCl. For applied potentials above the FBP, we observe $\Delta\omega_{\text{CN}} > 0$ (i.e., blue-shifts ~ 1 cm^{-1}) corresponding to positive photovoltages, whereas for applied potentials below the flat band potential, we observe $\Delta\omega_{\text{CN}} < 0$ (i.e., red-shifts ~ 1 cm^{-1}) corresponding to negative photovoltages. These spectroscopic observations reveal voltage-induced changes in the band bending at the semiconductor/liquid junction that, thus far, have been difficult to measure.

KEYWORDS: SERS, 4-MBN, band bending, photochemical, semiconductor–liquid surface

1. INTRODUCTION

Spectroscopic methods for determining the local electric field, local pH, charge transfer, and surface potential at electrode surfaces are becoming increasingly important tools for understanding photoelectrochemistry.^{1–3} Developing a clear picture of energy loss mechanisms in photocatalysis at semiconductor/liquid interfaces is particularly challenging because of band bending, built-in electric fields, surface and bulk recombination of photoexcited carriers, and ultimately charge transfer to the ions in solution, during which the electrostatic fields play an important role. Spectroscopic tools can provide quantitative measurements of key unknowns in photoelectrochemical processes at semiconductor/liquid interfaces. For example, the potential at a semiconductor surface is often not known under photoelectrochemical conditions.

In the study of photovoltages at semiconductor–electrolyte junctions, researchers have used a variety of methods to study and improve photoelectrochemical (PEC) devices.^{4,5} Tuning band energetics via surface dipoles holds promise for optimizing photovoltage, although achieving the desired outcomes often poses major challenges, including surface stability.^{6–9} Evaluating materials based on their external

Received: September 20, 2023

Revised: January 17, 2024

Accepted: January 17, 2024

radiative efficiency can be an important criterion for identifying good PEC electrodes; however, its effectiveness may be limited by other factors influencing the overall performance of PEC cells.^{10,11} Several research groups have reported rough photovoltage measurements by “eyeballing” the shift in the onset potential of semiconductor photoelectrodes under illumination with that of metal electrodes or heavily doped semiconductor electrodes of the opposite carrier type in the dark.^{12–14} Using this approach, the photovoltage produced at the semiconductor/liquid interface is not well-defined because the shift depends on the current at which the onset potential is defined (e.g., the photovoltage at 1 mA/cm² can be very different from the photovoltage at 10 mA/cm²). Other groups have reported open circuit potential (OCP) measurements.¹⁵ However, the open circuit potentials can be offset by large voltages due to electrochemical current from spurious reactions. Here, a slight offset in current can cause a large change in the OCP because the *I*–*V* curve is flat in this potential range. Measurements of quasi-Fermi-level splitting in semiconductor photoelectrodes have also been reported using similar techniques for tracking the potential of the minority carrier Fermi level as a function of changing electrode potential.^{16–19} However, these measurements suffer from the same inaccuracies, and in general, improved techniques are needed.

Surface-enhanced Raman spectroscopy (SERS) has emerged as a promising technique for *in situ* investigation of a diverse range of physical and chemical properties. In recent research, SERS was utilized to detect charge transfer occurring in ferrocene/ferrocenium (Fc/Fc⁺) moieties anchored to an active electrode operating under electrochemical working conditions. This approach provided insights into the fundamental mechanism of electron transfer transpiring at the electrode interface, which for Fc/Fc⁺ occurs at a well-defined redox potential (i.e., +0.4 V vs Ag/AgCl). SERS has also been used to measure quasi-Fermi-level alignment of metal catalyst sites within heterogeneous metal–insulator–semiconductor (MIS) photoelectrodes.³ This allowed for an estimation of the photovoltage at these sites; however, they did not consider the static charge trapped in the oxide/semiconductor surface and did not establish any correlation between photovoltages and laser power. In addition, they solely focused on Fermi-level alignment but did not discuss band bending. Earlier techniques on metal electrodes have involved the utilization of surface-bound thiolated molecules like 4-mercaptobenzonitrile (4-MBN), which play a pivotal role in this spectroscopic method.^{2,21} 4-MBN is also a commonly employed spectral reporter for assessing electric fields in proteins.^{21,22}

In our study, we observe variations in the MBN vibrational frequency induced under different laser powers to indicate changes in the semiconductor band bending under various applied electrochemical voltages. These findings were then integrated to yield a photovoltage of approximately 400 mV. The *in situ* Raman measurements presented here provide insight into the band bending and electrostatic charge distributions at the semiconductor/metal oxide/liquid interface, which is quite sensitive to the applied electrochemical potential.

2. MATERIALS AND METHODS

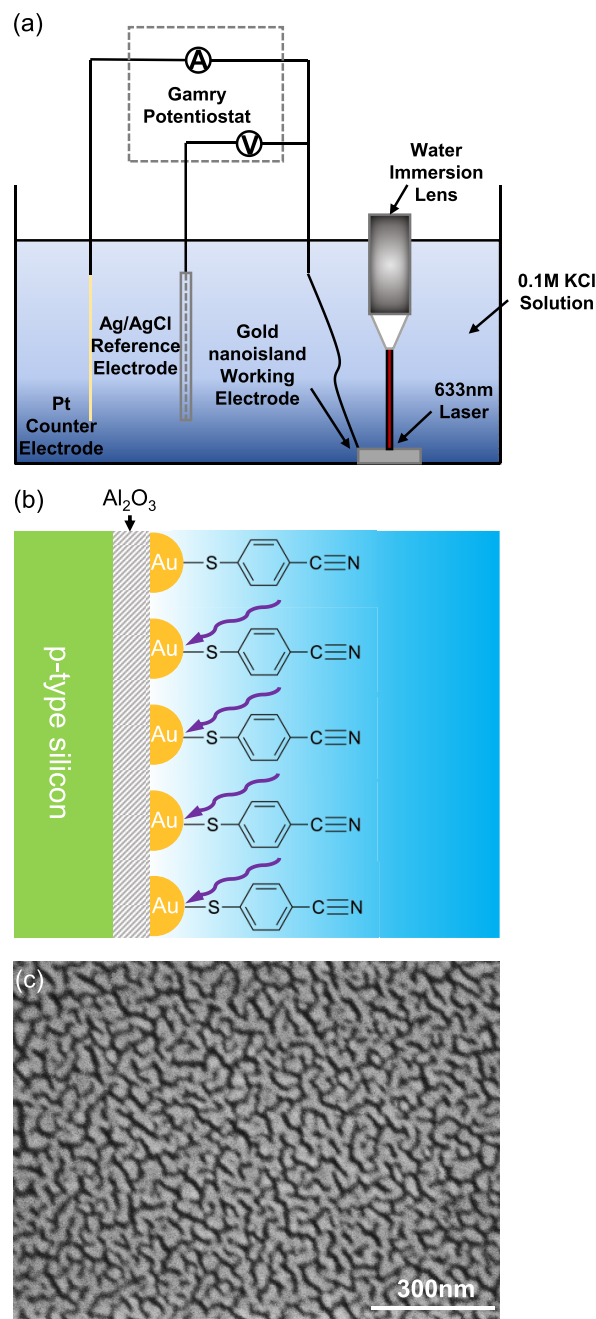


Figure 1. (a) Schematic diagram of the *in situ* Raman measurements using a water immersion lens and a three-terminal potentiostat. (b) Cross-sectional diagram of 4-mercaptobenzonitrile (4-MBN) bonded to Au nanosilver islands deposited on p-type silicon with an alumina protective layer. (c) SEM image of the Au nanosilver island.

conditions. A water immersion lens (Leica model HC APO L 102 #506155 40×, N.A. = 0.8) is used for the measurements. The working electrode, illustrated in Figure 1b, is a SERS-active electrode used in conjunction with a Pt counter electrode (26 gauge, 99.9%) and a Ag/AgCl reference electrode (BASi, MF-2052). Various electrode potentials are applied using a Gamry potentiostat (Reference 600+), which is also used to obtain Mott–Schottky plots (i.e., $1/C^2$ vs potential) at 15 kHz with a 50 mV rms AC voltage. Raman spectra are collected using a Renishaw inVia micro-Raman spectrometer with a 633 nm wavelength laser (Cobolt, 08-NLD). The integration time for Raman spectra collection is 1 min, and the incident laser power is maintained at 0.93 mW. To prepare the sample shown in Figure 1b, p-type silicon with a resistivity in the range 1–100 Ω·cm (University

The schematic diagram illustrated in Figure 1a depicts *in situ* Raman spectroscopy of the electrode surfaces under working electrochemical

115 Wafer) is soaked in buffered oxide etchant (BOE) 10:1 (Sigma-
 116 Aldrich, #901621) for 45 s to remove the native silicon dioxide from
 117 both sides. Subsequently, a 50 nm gold layer (with a 5 nm titanium
 118 adhesion layer) is deposited as a back contact using electron-beam
 119 evaporation. On the top side of the wafer, a 5 nm Al_2O_3 layer is grown
 120 at 200 °C using atomic-layer deposition (ALD). Trimethylaluminum
 121 (TMA, $\text{Al}(\text{CH}_3)_3$) is used as the metal precursor and H_2O as a
 122 coreactant, which yields 1 per cycle. Additionally, a 7 nm gold layer is
 123 deposited on the same side using electron beam evaporation, which
 124 produces a nanoisland structure (shown in Figure 1c) that gives rise
 125 to strong plasmonic hot spots and large SERS enhancement factors, as
 126 described in detail in our previous works (see Figure S1).^{20,23–25} To
 127 conduct the SERS measurements, 4-MBN (4-mercaptobenzonitrile
 128 available from Sigma-Aldrich, #A514431) is chemisorbed onto the Au
 129 nanoislands. This is achieved by immersing the substrate in a 30 mM
 130 mixture of 4-MBN in ethanol for 24 h. The samples are then rinsed in
 131 ethanol and immersed in an aqueous solution of 0.1 M KCl for the
 132 measurements shown in Figure 2.

3. RESULTS AND DISCUSSION

133 Figure 2a shows the raw Raman spectra of the $\text{C}\equiv\text{N}$ stretch
 134 mode of surface-bound MBN taken under various applied
 135 electrochemical potentials. Here, we see two trends in the data.
 136 First, there is a red-shift of the ω_{CN} peak at lower (more
 137 reducing) potentials. This trend is plotted in Figure 2b and
 138 corresponds to a Stark-tuning rate of $d\omega/dV = 5.74 \text{ cm}^{-1}/\text{V}$.
 139 In air, we measured the nitrile stretch mode frequency to be
 140 2225.3 cm^{-1} , as shown in Figure S2, which is consistent with
 141 Schkolnik et al.'s previous work.²¹ The in-air vibrational
 142 frequency corresponds to the zero electric field conditions
 143 because there are no ions present to create an electric field. It is
 144 interesting that the point of zero field is not coincident with
 145 the inversion point of the photovoltages (from negative to
 146 positive). This may indicate that the electrostatics and energy
 147 equilibration at the semiconductor–liquid interface are further
 148 complicated by the presence of the metal oxide layer. Second,
 149 there is a clear increase in the Raman intensity of the $\text{C}\equiv\text{N}$
 150 peak. This trend is plotted in Figure 2c, reaching a 2-fold
 151 increase in intensity at $V = -0.8 \text{ V}$ vs Ag/AgCl, and arises due
 152 to the change in the tilt angle θ of the nitrile bond of the 4-
 153 MBN molecules closer to the surface normal, as discussed by
 154 Schkolnik et al.²¹ Additional measurements were performed in
 155 a 1 M HCl solution, which resulted in similar trends, as shown
 156 in Figures S3 and S4 of the Supporting Information.

157 Figure 3a shows the laser power dependence of the $\text{C}\equiv\text{N}$
 158 stretch vibrational frequency (i.e., ω_{CN}) measured under
 159 various applied electrochemical potentials in the range from
 160 0 to -0.7 V vs Ag/AgCl. These vibrational Stark shifts describe
 161 the change in vibrational frequency of a molecule in response
 162 to an external electric field.²⁶ These Raman frequency shifts
 163 $\Delta\omega_{\text{CN}}$ can be converted to electric field using the relation $E =$
 164 $\Delta\omega_{\text{CN}}^0/0.36 [(\text{MV}/\text{cm})/\text{cm}^{-1}]$,²⁹ which is plotted on the right
 165 y-axis in Figure 3a.^{27,28} Here, we see two trends in the data.
 166 Above -0.39 V , ω_{CN} increases (i.e., blue-shifts) with increasing
 167 laser power, indicating a shift in the surface potential to higher
 168 (more oxidizing) potentials, as established in Figure 2b. Below
 169 -0.39 V , ω_{CN} decreases (i.e., red-shifts) with increasing laser
 170 power, indicating a shift in the surface potential to lower (more
 171 reducing) potentials. The maximum photoinduced change in
 172 the Raman shift (i.e., $\Delta\omega_{\text{CN}}$) is plotted in Figure 3b as a
 173 function of the applied electrochemical potential. The
 174 corresponding photovoltage, derived from the relation
 175 $\Delta V = \Delta\omega_{\text{CN}}/(d\omega/dV)$ with a slope of $d\omega/dV = 5.76$, was
 176 obtained from Figure 2b and is plotted on the right-hand y-axis

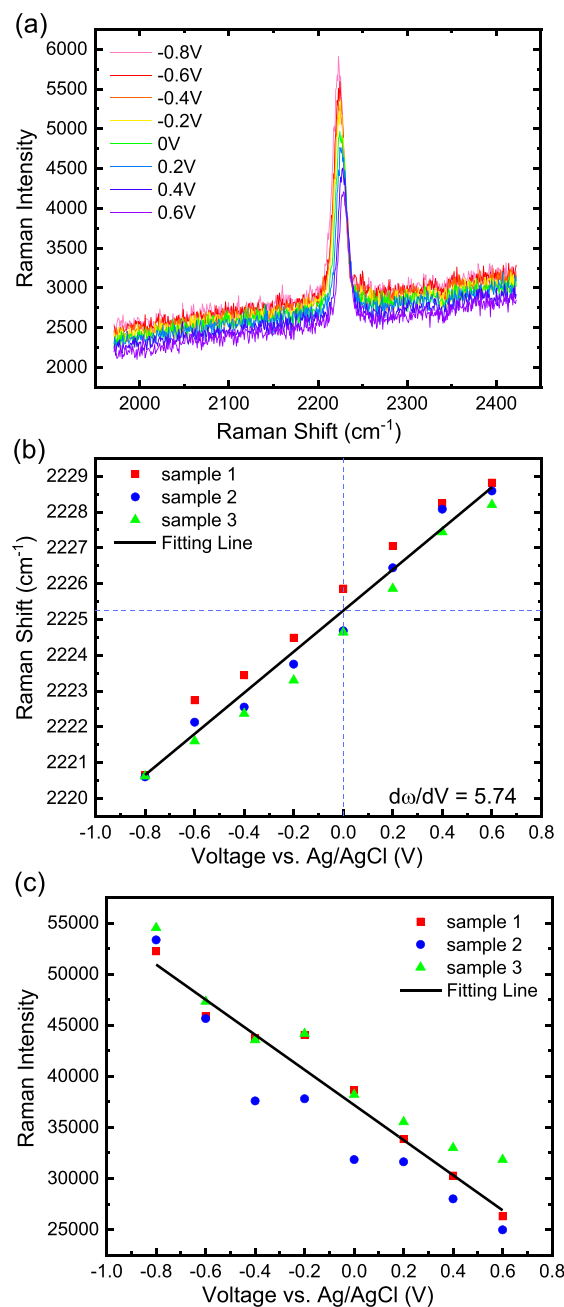


Figure 2. (a) Raw Raman spectra taken in 0.1 M KCl solution under various applied potentials. (b) Raman shift and (c) Raman intensity of the $\text{C}\equiv\text{N}$ stretch mode plotted as a function of the applied electrochemical potential.

of this graph, spanning the range from -0.18 to $+0.20 \text{ V}$. Both the photovoltage (ΔV) and photoinduced change in the Raman frequency ($\Delta\omega_{\text{CN}}$) invert from negative to positive values above -0.39 V vs Ag/AgCl, which corresponds to the flat band potential. Figure 3c shows a Mott–Schottky plot of $1/C^2$ vs potential exhibiting an x -intercept of -0.39 V vs Ag/AgCl. This indicates the position of the flat band potential and is consistent with the inversion points measured in Figures 3a and 3b. In addition, we verified the reversibility of these signals by repeating the laser power-dependent measurement several times. This data is plotted in Figure S5 of the Supporting Information.

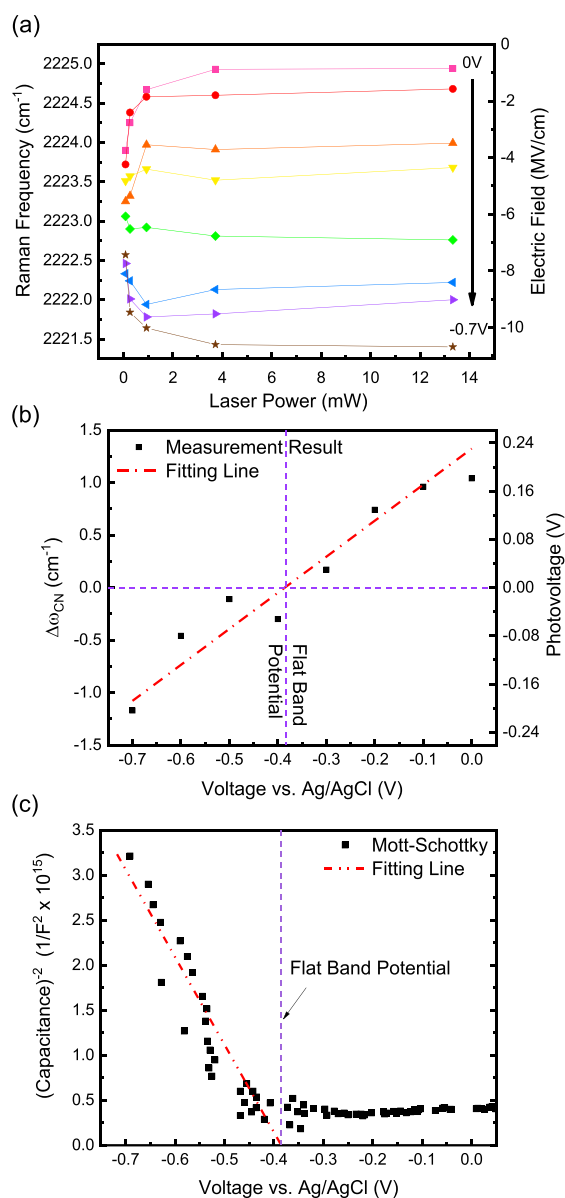


Figure 3. (a) Raman shifts of the C≡N stretch mode taken under various applied potentials plotted as a function of laser power. (b) Maximum photoinduced change in Raman shift ($\Delta\omega_{CN}$) and corresponding photovoltage plotted as a function of applied potential. (c) Mott–Schottky plot and linear fit, indicating the flat band potential.

ions in solution further increase the depletion region and built-in field. However, this is highly dependent on the applied electrochemical potential and can span a range from depletion to flat band and ultimately to accumulation conditions.

The *in situ* Raman measurements presented above provide insight into the band bending and electrostatic charge distributions at the semiconductor/metal oxide/liquid interface. Figures 4a–c show energy band diagrams of the semiconductor/metal oxide/liquid interface under depletion, flat band, and accumulation conditions. Under low negative applied potentials (i.e., $V < -0.4$ V vs Ag/AgCl), the H^+ ions in solution produce a large amount of band bending and an associated depletion region that sweeps photogenerated minority carriers out to the ions in solution, as illustrated in Figure 4a. However, this band bending phenomenon is a strong function of the applied electrochemical potential. The applied potential of $V = -0.4$ V vs Ag/AgCl corresponds to the flat band potential and is illustrated in Figure 4b. For potentials above this, i.e., $V > -0.4$ V vs Ag/AgCl, the semiconductor moves into the accumulation regime, in which majority carrier holes form an accumulation region at the surface of the semiconductor, as illustrated in Figure 4c. While the electrostatics of the Al_2O_3 layer further complicate the behavior of this interface, these *in situ* photovoltage measurements enable us to explore the band inversion that takes place in the underlying silicon semiconductor.

Some recent theoretical studies report a direct link between the SERS signal and charge transfer; however, this is likely to be negligible compared to the charge transfer produced by the underlying semiconductor.^{30,31} We utilized the plasmon resonance of the gold nanoparticles to provide SERS enhancement. However, any electrochemical effects associated with these plasmons will likely be negligible compared to those of the photovoltages produced by the underlying semiconductor. That is the plasmon resonance associated with these gold nanoparticles provides strong electric field enhancement (i.e., $E^2 \sim 10^6$) at optical frequencies, but photovoltages associated with these plasmons will be much smaller than those produced by the semiconductor.^{24,32} The linear trend observed in the photovoltage as a function of the applied potential (Figure 3b) is expected for potentials below the flat band potential, and the photovoltage of zero corresponding to the flat band potential also makes sense. However, the linear trend in photovoltage for potentials above the flat band potential is not fully understood. There are numerous factors that can change both above and below the flat band potential, including the following: (1) The fraction of applied potential that is distributed across the semiconductor, as opposed to across the Helmholtz layer, will vary with applied potential and have different values depending on whether there is “depletion” or “accumulation” at the semiconductor surface. (2) The net charge on the metal oxide layer can change from positive to negative above and below the FBP. (3) The dominant half-reaction responsible for Fermi-level pinning can change above and below the FBP. Furthermore, the simple interpretation of the flat band potential, as extracted from the Mott–Schottky measurements, is based on a single capacitor model. It is likely that the metal oxide layer introduces a second capacitor in series with the one associated with the depletion region in the silicon semiconductor, further complicating our interpretation. It is important to note that the photovoltage, here, is not measured with respect to “dark” conditions but with respect to low light levels. Therefore, essentially what we are measuring

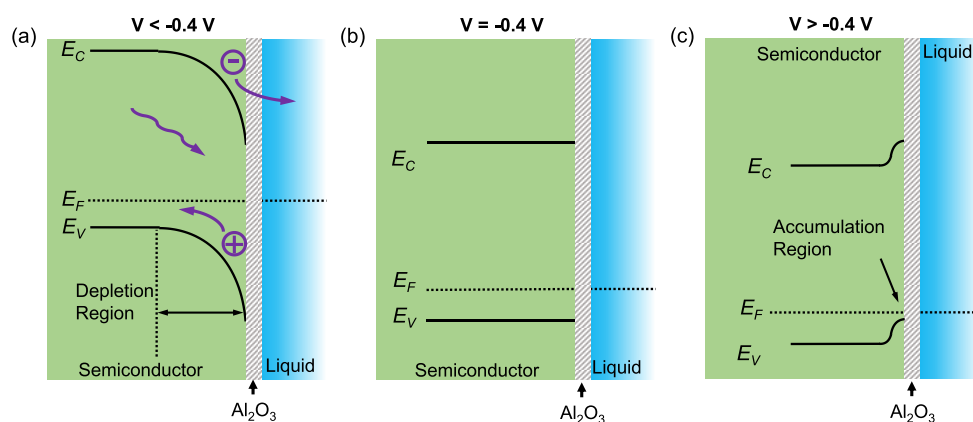


Figure 4. Energy band diagrams of the p-Si/Al₂O₃/electrolyte solution under applied potentials (a) less than −0.4 V vs Ag/AgCl, (b) at −0.4 V vs Ag/AgCl (i.e., flat band potential), and (c) above −0.4 V vs Ag/AgCl.

(in Figures 3a and 3b) is the difference in photovoltage between high light levels and low light levels. As such, the effects of band flattening could play a role in the observed photovoltage response of the system. The data presented in Figure 3b have been repeated several times and indicate that our understanding of metal oxide-protected semiconductors must be revisited, and further measurements via *in situ* spectroscopy techniques (e.g., transient reflectance spectroscopy) will be needed in order to obtain a complete understanding of this interesting photoelectrode system.

There are two perspectives from which to view the semiconductor/liquid junction. One is based on energy equilibration (i.e., the Fermi level in the semiconductor aligns with the dominant half-reaction in the electrochemical system), and the other is based on electrostatics (i.e., the capacitance associated with the depletion region in the semiconductor and charge/ion accumulation in the solution). Figure S8 illustrates these two perspectives. In essence, the solution has an effect on the photovoltage of the Si/Al₂O₃ system because the accumulation of anions increases the band bending, which, in turn, increases the photovoltage. While there are many functional groups on the photoelectrode surface such as OH, OOH, Cl, and H, for large negative potentials, we expect the dominant reduction half-reaction to be HER. For high positive potentials, we expect the dominant half-reaction to be OER. In the intermediate range, it is unclear which redox couple is pinning the Fermi level.

4. CONCLUSION

In conclusion, we utilized a spectroscopic technique for tracking the photovoltages generated at junctions between semiconductors and liquid electrolytes. In this method, the reporter molecule mercaptobenzonitrile (MBN) is functionalized on the surface of the photoelectrode. The measurements are performed using *in situ* SERS spectroscopy through a water immersion lens while the photoelectrochemical processes are initiated. Specifically, the vibrational frequency of the C≡N stretch mode (ω_{CN}) is responsive to the local electric field in the solution at the interface between the electrode and the electrolyte due to the vibrational Stark effect. Within the range of applied potentials spanning from −0.8 to 0.6 V vs Ag/AgCl, the ω_{CN} value shifts from 2220 to 2229 cm^{−1} (at low laser power). As the incident laser power is increased from 83.5 μW to 13.3 mW, additional shifts of approximately ± 1 cm^{−1} are observed. These shifts correspond to the photovoltages

produced at the interface between the semiconductor and the liquid, resulting in voltage changes of approximately ± 0.2 V. Based on Mott–Schottky measurements, the flat band potential (FBP) emerges at −0.39 V compared to the Ag/AgCl reference electrode. When the applied potentials surpass the FBP, the ω_{CN} values exhibit positive shifts (blue-shifts) of around 1 cm^{−1}, indicating positive photovoltages. Conversely, when the applied potentials fall below the flat band potential, the ω_{CN} values display negative shifts (red-shifts) of approximately 1 cm^{−1}, corresponding to negative photovoltages. These spectroscopic findings suggest a voltage-driven reversal in the band bending at the junction between the semiconductor and the liquid, a phenomenon that has previously proven to be elusive and challenging to measure. At semiconductor/liquid interfaces, both the surface potential and photovoltage are influenced by a combination of band bending and quasi-Fermi-level splitting at the semiconductor surface. These factors are often addressed in a qualitative manner, highlighting the importance of devising quantitative metrics for assessing the band energies and photovoltages at these interfaces.

■ ASSOCIATED CONTENT

Supporting Information

The Supporting Information is available free of charge at <https://pubs.acs.org/doi/10.1021/acsami.3c14116>.

Measured Raman spectra taken in air, in 1 M HCl solution, and additional data sets taken on a different sample; schematic diagram of the surface depletion in p-type silicon (PDF)

■ AUTHOR INFORMATION

Corresponding Author

Stephen B. Cronin – Ming Hsieh Department of Electrical Engineering, University of Southern California, Los Angeles, California 90089, United States; orcid.org/0000-0001-9153-7687; Email: scronin@usc.edu

Authors

Ruoxi Li – Mork Family Department of Chemical Engineering and Materials Science, University of Southern California, Los Angeles, California 90089, United States; orcid.org/0000-0002-6432-6072

350 **Marcos Gabriel Yoc-Bautista** – Department of Chemistry,
351 Haverford College, Haverford, Pennsylvania 19041, United
352 States

353 **Sizhe Weng** – Ming Hsieh Department of Electrical
354 Engineering, University of Southern California, Los Angeles,
355 California 90089, United States; [orcid.org/0000-0002-](https://orcid.org/0000-0002-6555-2442)
356 [6555-2442](https://orcid.org/0000-0002-6555-2442)

357 **Zhi Cai** – Mork Family Department of Chemical Engineering
358 and Materials Science, University of Southern California, Los
359 Angeles, California 90089, United States; [orcid.org/](https://orcid.org/0000-0002-3741-5715)
360 [0000-0002-3741-5715](https://orcid.org/0000-0002-3741-5715)

361 **Bofan Zhao** – Ming Hsieh Department of Electrical
362 Engineering, University of Southern California, Los Angeles,
363 California 90089, United States; [orcid.org/0000-0003-](https://orcid.org/0000-0003-0478-6330)
364 [0478-6330](https://orcid.org/0000-0003-0478-6330)

365 Complete contact information is available at:

366 <https://pubs.acs.org/10.1021/acsami.3c14116>

367 Notes

368 The authors declare no competing financial interest.

369 ■ ACKNOWLEDGMENTS

370 This research was supported by the U.S. Department of
371 Energy, Office of Basic Energy Sciences, award DESC0019322.
372 The authors also acknowledge the NSF Research Experiences
373 for Undergraduates (REU) program award CHE-1757942
374 (M.G.Y.).

375 ■ REFERENCES

- 376 (1) Li, R.; Chaudhry, I.; Tseng, C.; Weng, S.; Wang, Y.; Zhao, B.;
377 Aravind, I.; Cai, Z.; Dawlaty, J.; Jensen, L.; Cronin, S. B. SERS
378 Detection of Charge Transfer at Electrochemical Interfaces Using
379 Surface-Bound Ferrocene. *J. Phys. Chem. C* **2023**, *127*, 14263.
380 (2) Sarkar, S.; Patrow, J. G.; Voegtli, M. J.; Pennathur, A. K.;
381 Dawlaty, J. M. Electrodes as polarizing functional groups: Correlation
382 between Hammett parameters and electrochemical polarization. *J.*
383 *Phys. Chem. C* **2019**, *123* (8), 4926–4937.
384 (3) Suo, S.; Sheehan, C.; Zhao, F.; Xiao, L.; Xu, Z.; Meng, J.;
385 Mallouk, T. E.; Lian, T. Direct Vibrational Stark Shift Probe of Quasi-
386 Fermi Level Alignment in Metal Nanoparticle Catalyst-Based Metal–
387 Insulator–Semiconductor Junction Photoelectrodes. *J. Am. Chem. Soc.*
388 **2023**, *145*, 14260.
389 (4) Cowan, A. J.; Durrant, J. R. Long-lived charge separated states in
390 nanostructured semiconductor photoelectrodes for the production of
391 solar fuels. *Chem. Soc. Rev.* **2013**, *42* (6), 2281–2293.
392 (5) Hu, L.; Mandelis, A. Advanced characterization methods of
393 carrier transport in quantum dot photovoltaic solar cells. *J. Appl. Phys.*
394 **2021**, *129* (9), 091101.
395 (6) Guijarro, N.; Prévot, M. S.; Sivula, K. Surface modification of
396 semiconductor photoelectrodes. *Phys. Chem. Chem. Phys.* **2015**, *17*
397 (24), 15655–15674.
398 (7) MacLeod, B. A.; Steirer, K. X.; Young, J. L.; Koldemir, U.;
399 Sellinger, A.; Turner, J. A.; Deutsch, T. G.; Olson, D. C. Phosphonic
400 acid modification of GaInP₂ photocathodes toward unbiased
401 photoelectrochemical water splitting. *ACS Appl. Mater. Interfaces*
402 **2015**, *7* (21), 11346–11350.
403 (8) Smith, W. A.; Sharp, I. D.; Strandwitz, N. C.; Bisquert, J.
404 Interfacial band-edge energetics for solar fuels production. *Energy*
405 *Environ. Sci.* **2015**, *8* (10), 2851–2862.
406 (9) Boucher, D. G.; Kearney, K.; Ertekin, E.; Rose, M. J. Tuning p-Si
407 (111) Photovoltage via Molecule Semiconductor Electronic Cou-
408 pling. *J. Am. Chem. Soc.* **2021**, *143* (6), 2567–2580.
409 (10) Fountaine, K. T.; Lewerenz, H. J.; Atwater, H. A. Efficiency
410 limits for photoelectrochemical water-splitting. *Nat. Commun.* **2016**, *7*
411 (1), No. 13706.

(11) Green, M. A. Radiative efficiency of state-of-the-art photo-
voltaic cells. *Progress in Photovoltaics: Research and Applications* **2012**,
20 (4), 472–476.

(12) Hu, S.; Shaner, M. R.; Beardslee, J. A.; Lichterman, M.;
Brunschwig, B. S.; Lewis, N. S. Amorphous TiO₂ coatings stabilize Si,
GaAs, and GaP photoanodes for efficient water oxidation. *Science*
2014, *344* (6187), 1005–1009.

(13) Hemmerling, J.; Quinn, J.; Linic, S. Quantifying Losses and
Assessing the Photovoltage Limits in Metal–Insulator–Semiconduc-
tor Water Splitting Systems. *Adv. Energy Mater.* **2020**, *10* (12),
No. 1903354.

(14) Hemmerling, J. R.; Mathur, A.; Linic, S. Design Principles for
Efficient and Stable Water Splitting Photoelectrocatalysts. *Acc. Chem.*
Res. **2021**, *54* (8), 1992–2002.

(15) Hu, S.; Richter, M. H.; Lichterman, M. F.; Beardslee, J.; Mayer,
T.; Brunschwig, B. S.; Lewis, N. S. Electrical, Photoelectrochemical,
and Photoelectron Spectroscopic Investigation of the Interfacial
Transport and Energetics of Amorphous TiO₂/Si Heterojunctions. *J.*
Phys. Chem. C **2016**, *120* (6), 3117–3129.

(16) Kenyon, C.; Tan, M. X.; Krüger, O.; Lewis, N. S. Behavior of Si
photoelectrodes under high level injection conditions. 3. Transient
and steady-state measurements of the quasi-Fermi levels at Si/
CH₃OH contacts. *J. Phys. Chem. B* **1997**, *101* (15), 2850–2860.

(17) Krüger, O.; Kenyon, C.; Tan, M. X.; Lewis, N. S. Behavior of Si
photoelectrodes under high level injection conditions. 2. Experimental
measurements and digital simulations of the behavior of quasi-Fermi
levels under illumination and applied bias. *J. Phys. Chem. B* **1997**, *101*
(15), 2840–2849.

(18) PINSON, W. E. Quasi-Fermi level measurement in an
illuminated GaP photoelectrolysis cell. *Nature* **1977**, *269* (5626),
316–318.

(19) Tan, M. X.; Kenyon, C.; Lewis, N. S. Experimental
measurement of quasi-fermi levels at an illuminated semiconductor/
liquid contact. *J. Phys. Chem.* **1994**, *98* (19), 4959–4962.

(20) Li, R.; Chaudhry, I.; Tseng, C.; Weng, S.; Wang, Y.; Zhao, B.;
Aravind, I.; Cai, Z.; Dawlaty, J.; Jensen, L.; Cronin, S. B. SERS
Detection of Charge Transfer at Electrochemical Interfaces Using
Surface-Bound Ferrocene. *J. Phys. Chem. C* **2023**, *127*, 14263.

(21) Schkolnik, G.; Salewski, J.; Millo, D.; Zebger, I.; Franzen, S.;
Hildebrandt, P. Vibrational Stark effect of the electric-field reporter 4-
mercaptobenzonitrile as a tool for investigating electrostatics at
electrode/SAM/solution interfaces. *International journal of molecular*
sciences **2012**, *13* (6), 7466–7482.

(22) Schkolnik, G.; Utesch, T.; Salewski, J.; Tenger, K.; Millo, D.;
Kranich, A.; Zebger, I.; Schulz, C.; Zimanyi, L.; Rakhely, G.;
Mrogiński, M. A.; Hildebrandt, P. Mapping local electric fields in
proteins at biomimetic interfaces. *Chem. Commun.* **2012**, *48* (1), 70–
72.

(23) Chen, J.; Bailey, C. S.; Hong, Y.; Wang, L.; Cai, Z.; Shen, L.;
Hou, B.; Wang, Y.; Shi, H.; Sambur, J.; Ren, W.; Pop, E.; Cronin, S. B.
Plasmon-resonant enhancement of photocatalysis on monolayer
WSe₂. *ACS Photonics* **2019**, *6* (3), 787–792.

(24) Shen, L.; Gibson, G. N.; Poudel, N.; Hou, B.; Chen, J.; Shi, H.;
Guignon, E.; Cady, N. C.; Page, W. D.; Pilar, A.; Cronin, S. B.
Plasmon resonant amplification of hot electron-driven photocatalysis.
Appl. Phys. Lett. **2018**, *113* (11), 113104 DOI: [10.1063/1.5048582](https://doi.org/10.1063/1.5048582).

(25) Shi, H.; Pekarek, R. T.; Chen, R.; Zhang, B.; Wang, Y.; Aravind,
I.; Cai, Z.; Jensen, L.; Neale, N. R.; Cronin, S. B. Monitoring Local
Electric Fields using Stark Shifts on Naphthyl Nitrile-Functionalized
Silicon Photoelectrodes. *J. Phys. Chem. C* **2020**, *124* (31), 17000–
17005.

(26) Bagchi, S.; Fried, S. D.; Boxer, S. G. A solvatochromic model
calibrates nitriles' vibrational frequencies to electrostatic fields. *J. Am.*
Chem. Soc. **2012**, *134* (25), 10373–10376.

(27) Fried, S. D.; Boxer, S. G. Measuring electric fields and
noncovalent interactions using the vibrational Stark effect. *Acc. Chem.*
Res. **2015**, *48* (4), 998–1006.

(28) Patrow, J. G.; Sorenson, S. A.; Dawlaty, J. M. Direct
spectroscopic measurement of interfacial electric fields near an

481 electrode under polarizing or current-carrying conditions. *J. Phys.*
482 *Chem. C* **2017**, *121* (21), 11585–11592.

483 (29) Sorenson, S. A.; Patrow, J. G.; Dawlaty, J. M. Solvation reaction
484 field at the interface measured by vibrational sum frequency
485 generation spectroscopy. *J. Am. Chem. Soc.* **2017**, *139* (6), 2369–
486 2378.

487 (30) Ngo, T. C.; Trinh, Q. T.; Thi Thai An, N.; Tri, N. N.; Trung,
488 N. T.; Truong, D. H.; Huy, B. T.; Nguyen, M. T.; Dao, D. Q. SERS
489 spectra of the pesticide chlorpyrifos adsorbed on silver nanosurface:
490 the Ag₂₀ cluster model. *J. Phys. Chem. C* **2020**, *124* (39), 21702–
491 21716.

492 (31) Dao, D. Q.; Ngo, T. C.; Le, T. T. H.; Trinh, Q. T.; Nguyen, T.
493 L. A.; Huy, B. T.; Tri, N. N.; Trung, N. T.; Nguyen, M. T. SERS
494 chemical enhancement of 2, 4, 5-trichlorophenoxyacetic acid
495 adsorbed on silver substrate. *J. Phys. Chem. A* **2021**, *125* (39),
496 8529–8541.

497 (32) Wang, Y.; Aravind, I.; Cai, Z.; Shen, L.; Gibson, G. N.; Chen, J.;
498 Wang, B.; Shi, H.; Song, B.; Guignon, E.; Cady, N. C.; Page, W. D.;
499 Pilar, A.; Cronin, S. B. Hot electron driven photocatalysis on plasmon-
500 resonant grating nanostructures. *ACS Appl. Mater. Interfaces* **2020**, *12*
501 (15), 17459–17465.